Applied Ocean Research 150 (2024) 104125

Contents lists available at ScienceDirect

Applied Ocean Research

journal homepage: www.elsevier.com/locate/apor

Research paper

# Nonlinear wave resonance by four bottom-mounted cylinders in a uniform current using a higher order finite element method

C.Z. Wang [a,c], J.M. Ren [a], Y.F. Yang [a,b], H. Ge [a,*]

[a] Ocean College, Zhejiang University, Zhoushan 316021, China
[b] Department of Mechanical Engineering, University College London, Torrington Place, London WC1E 7JE, United Kingdom
[c] Yangjiang Offshore Wind Power Laboratory, Yangjiang 529500, China

ARTICLE INFO

*Keywords:*
Wave resonance
Nonlinear wave-current-body interaction
Multiple cylinders
Potential flow theory
Higher order finite element method

ABSTRACT

The fully nonlinear wave potential theory is employed to analyze interactions of water waves and a group or an array of vertical cylinders in a uniform current in three-dimensions (3D). The nonlinear free surface boundary conditions are satisfied on the transient position. The velocity potential at each time step are solved through a higher order finite element method (HOFEM) with hexahedral 20-node parametric elements and the velocity on the free surface are obtained by differentiating the shape functions directly. The radiation condition is imposed through a damping zone method. Wave resonance for four bottom mounted cylinders at near-trapping modes is simulated with considering current effect. Waves and hydrodynamic forces are obtained to show their resonant behaviors at different current speeds and different incident wave amplitudes. Comparisons are also made with those by previous study and the time-domain second order solutions and agreement and disagreement are discussed between them.

## 1. Introduction

Over the last decades, with the increasing demands of energy resource, more and more attention has been paid to oil exploitation in ocean especially in deep sea. There has been extensive research into interactions between water waves and ocean structures, most of which consist of multiple bodies such as a group or an array of vertical cylinders. An interesting problem is the trapped wave, which is a resonant phenomenon when the interactions between waves and ocean structures with multi-body happen at some special wave frequencies. Maniar and Newman (1997) investigated linear wave diffraction by an array of 101 circular cylinders in the frequency domain. They found that very large hydrodynamic forces could occur on the cylinders in the middle when the wave number was close to the trapped mode (Ursell, 1951). Newman (2001) also discussed wave resonance may happen in diffraction by an array of cylinder in other configurations. Evans and Porter (1997b) and Evans and Porter (1997a) founded that large force could occur for linear wave diffraction by a small number of circular cylinders, such as four, especially when they were quite close to each other. Malenica et al. (1999) further showed that similar behavior could occur for the second order solution, which were found to be abnormally large. Wang and Wu (2007) further made simulations based on the second order theory in the time domain and came to similar conclusions to above works based on the frequency domain theory. The near-trapping phenomenon of wave acting on multiple elliptical cylinders was investigated by Chen and Lee (2013) and Chatjigeorgiou and Katsardi (2018). Other investigations on wave interactions with an group of circular cylinders include those by Kashiwagi and Ohwatari (2002), Ohl et al. (2001), Kagemoto et al. (2014), Walker and Taylor (2005), Walker et al. (2008) and Grice et al. (2013).

While the perturbation theory can capture some important features of resonance, it does not always provide accurate results quantitatively. The main reason for this is that the perturbation theory is based on small parameter expansion. At resonance, the motion becomes very large. In fact, the motion can become infinite based on the linear and second order theories when there is no damping in the system. The actual situation may be much different between the linear or second order results and the fully nonlinear ones such as comparisons of radiation problems by floating bodies undergoing forced motions based on the second order theory by Wang and Wu (2008) and fully nonlinear theory by Wang et al. (2011) and Wang et al. (2013). This clearly contradicts with the foundation of the perturbation theory. Thus, an appropriate approach at resonance is to use the fully nonlinear theory. The nonlinear theory has been used previously for the resonant behavior of a sloshing tank in 3D

* Corresponding author.
*E-mail address:* gehan@zju.edu.cn (H. Ge).

https://doi.org/10.1016/j.apor.2024.104125
Received 19 September 2023; Received in revised form 22 June 2024; Accepted 8 July 2024

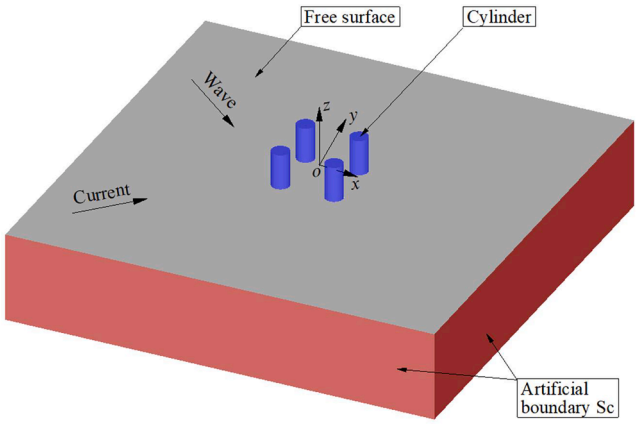


**Fig. 1.** A sketch of numerical wave tank.

by Wu et al. (1998) and two-dimensions (2D) by Wang and Khoo (2005). Wang and Wu (2010) reported wave mutual interference between multiple cylinders in a tank, in which the effects of tank wall on the wave and force are discussed and the resonant effects on waves and forces at the near-trapping mode frequency are also observed. Bai et al. (2014) reported near-trapping phenomenon for four vertical cylinders in waves and they strongly suggested that wave nonlinearity should be considered when studying multiple structures. Ning et al. (2015) and Feng and Bai (2015) considered wave resonance by multiple bodies in narrow gap in 2D and 3D. Li and Zhang (2016) simulated two barges in specified motions and calculated the response amplitude operator at resonant frequencies. Shivaji and Sen (2016) studied 3D gap resonance caused by side-by-side floating bodies using a mixed Eulerian–Lagrangian panel method.

The works mentioned above did not consider the current effect. Extensive studies for wave interactions with a single isolated body in a steady current can be found. For examples, second order simulations by Büchmann et al. (1998), Skourup et al. (2000), Shao and Faltinsen (2010) and Shao and Faltinsen (2013) and fully nonlinear studies by Büchmann et al. (2000), Celebi (2001), Ferrant (2001) and Koo and Kim (2007). However, little work has been done for multi-structures. Kim and Kim (1997) studied linear diffraction by four bottom-mounted cylinders but did not consider the nonlinear effect and the influence of current on near-trapping phenomenon. Recently, Huang and Wang (2019) simulated two-dimensional wave resonance by two rectangular barges in forced motions at different current speeds based on the second order theory in time domain and they found the linear and second waves amplitude decreases as the current speed increases in most cases, and this problem was further investigated by Huang et al. (2022) through the fully nonlinear potential flow theory and they found that the wave peaks and forces at resonant frequencies are clearly affected by the current speed. Yang and Wang (2020) considered the near-trapping phenomenon around four vertical bottom mounted cylinders in a steady current. Their investigation show that the first order wave or force increase as the increase of the Froude number but it is not clear for the second order at the trapped modes.

The present paper uses a higher order finite element method with hexahedral 20-node parametric elements to analyze the wave diffraction by four bottom-mounted cylinders in a uniform current in an open sea. The situation at the near-trapping frequencies is especially considered. The current effect on waves and hydrodynamic forces at the trapped modes are investigated and the nonlinear features at different incident wave amplitudes are also analyzed. The agreement and disagreement between the fully nonlinear and the perturbation methods within potential flow theory are discussed.

## 2. Mathematical formulation

We consider the wave interactions with a group of fixed cylinders in an open sea. As shown in Fig. 1, a right-handed Cartesian coordinate system *oxyz* is defined, in which *x* and *y* are measured horizontally and z points vertically upwards form the still water level. Each cylinder surface is denoted by $S_b$ and its unit normal vector directed outward from the fluid region is denoted by $\vec{n} = (n_x, n_y, n_z)$. The seabed is assumed horizontal along the plane $z = -h$. Let $t$ denote time and $\eta$ be the elevation of the free surface $S_f$relative to the still water level. When the fluid is assumed incompressible and inviscid, and the flow irrotational, the fluid motion can be described by a velocity potential $\varphi$ which satisfies the Laplace equation within the fluid domain $\forall$

$$\nabla^2\varphi = 0 \text{ in } \forall \tag{1}$$

For a problem with a uniform current with speed $\vec{U}$ along a direction at an angle $\beta_c$ with the *x*-axis, the total velocity potential is:

$$\Phi = \vec{U}\cdot\vec{x} + \varphi \tag{2}$$

where $\vec{U} = (U_x, U_y, 0) = (U\cos\beta_c, U\sin\beta_c, 0)$ and $\vec{x} = (x, y, 0)$. The potential $\Phi$ also satisfies the Laplace equation in the fluid domain and is subject to the following boundary conditions on the free surface $S_f$

$$\frac{\partial\eta}{\partial t} + \frac{\partial\Phi}{\partial x}\frac{\partial\eta}{\partial x} + \frac{\partial\Phi}{\partial y}\frac{\partial\eta}{\partial y} - \frac{\partial\Phi}{\partial z} = 0 \text{ on } S_f \tag{3}$$

$$\frac{\partial\Phi}{\partial t} = -g\eta - \frac{1}{2}|\nabla\Phi|^2 = 0 \text{ on } S_f \tag{4}$$

The condition on the cylinder surface can be expressed as

$$\frac{\partial\Phi}{\partial n} = 0 \text{ on } S_b. \tag{5}$$

since the cylinder is fixed. On the water bottom the boundary condition is

$$\frac{\partial\Phi}{\partial n} = 0 \text{ on } z = -h. \tag{6}$$

The boundary conditions mentioned above or Eqs. (3)~(6) may be expressed in terms of the disturbed potential $\varphi$ as

$$\frac{\partial\eta}{\partial t} + \left(U_x + \frac{\partial\varphi}{\partial x}\right)\frac{\partial\eta}{\partial x} + \left(U_y + \frac{\partial\varphi}{\partial y}\right)\frac{\partial\eta}{\partial y} - \frac{\partial\varphi}{\partial z} = 0 \text{ on } S_f \tag{7}$$

$$\frac{\partial\varphi}{\partial t} + g\eta + \frac{1}{2}|\nabla\varphi|^2 + \vec{U}\cdot\nabla\varphi = 0 \text{ on } S_f \tag{8}$$

$$\frac{\partial\varphi}{\partial n} = -\vec{U}\cdot\vec{n} \text{ on } S_b \tag{9}$$

$$\frac{\partial\varphi}{\partial n} = 0 \text{ on } z = -h \tag{10}$$

where $g$ is the acceleration due to gravity. In addition, the potential satisfies the radiation condition, which is imposed through a suitable numerical procedure applied on a control surface $S_c$ located at some distance away from the cylinder as shown in Fig. 1. In the present study, an artificial damping zone is placed near the truncated boundary $S_c$ to absorb the incoming wave and minimize the reflection, which will be hereinafter addressed.

In the present paper, the incident wave is chosen as the second order Stokes wave and its wave elevation and potential can be written as

$$\eta_I(x,y;t) = A\cos\theta + \frac{k}{4}A^2\frac{\cosh kh(\cosh 2kh + 2)}{\sinh^3 kh}\cos 2\theta \tag{11}$$

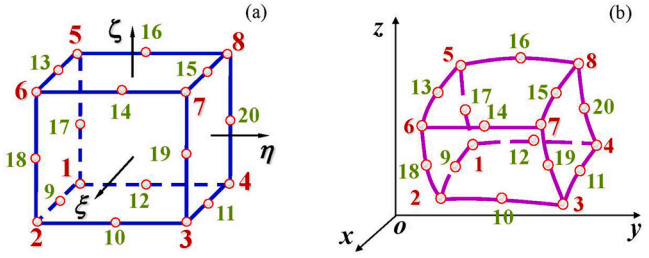


**Fig. 2.** Hexahedral 20-node parametric element.

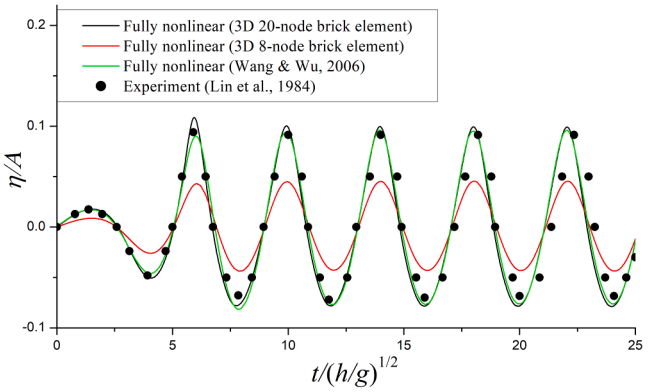


**Fig. 3.** Comparisons of waves between hexahedral 20- and 8-node parametric elements.

$$\varphi_I(x,y,z;t) = \frac{gA}{\omega}\frac{\cosh k(z+h)}{\cosh kh}\sin\theta + \frac{3}{8}A^2\omega\frac{\cosh 2k(z+h)}{\sinh^4 kh}\sin 2\theta, \tag{12}$$

where $A$, $\omega$ and $k$ is linear wave amplitude, frequency and wave number without current, respectively, and

$$\theta = k\ (x\cos\beta_w + y\sin\beta_w) - \omega_c t,$$

where $\omega_c = \omega + Uk\cos(\beta_c - \beta_w)$ is the frequency with considering the current effect or the encounter frequency.

Eqs. (7) and (8) can be written in Lagrangian form

$$\frac{Dx}{Dt} = \frac{\partial\varphi}{\partial x} + U_x,\quad \frac{Dy}{Dt} = \frac{\partial\varphi}{\partial y} + U_y,\quad \frac{Dz}{Dt} = \frac{\partial\varphi}{\partial z}, \tag{13}$$

$$\frac{D\varphi}{Dt} = -gz + \frac{1}{2}|\nabla\varphi|^2, \tag{14}$$

where $\frac{D}{Dt} = \frac{\partial}{\partial t} + \nabla\Phi\cdot\nabla$ is the material derivative.

Since the fully nonlinear water wave problem is solved in the time domain, the initial conditions including the position of the free surface $(x_0, y_0, z_0)$ and the velocity potential $\Phi_0$ or $\varphi_0$ on it should also be given, where $(x_0, y_0)$ is the node coordinate of a plane mesh on the static water level or $z = 0$ at the initial time step, and $z_0$ and $\Phi_0$ or $\varphi_0$ can be expressed as

$$\left.\begin{aligned} z_0 &= \eta_I(x_0,y_0;0)\\ \Phi_0 &= \varphi_I(x_0,y_0,0;0) + U\left(\cos\beta_c x_0 + \sin\beta_c y_0\right)\end{aligned}\right\}, \tag{15}$$

or

$$\left.\begin{aligned} z_0 &= \eta_I(x_0,y_0;0)\\ \varphi_0 &= \varphi_I(x_0,y_0,0;0)\end{aligned}\right\}, \tag{16}$$

respectively.

### 2.2. Evaluation of hydrodynamic forces

Once the velocity potential has been obtained through solving Eqs. (1), (13~14), (9~10) and (16), the pressure in the fluid can be determined by the Bernoulli equation

$$p = -\rho\left(\frac{\partial\varphi}{\partial t} + \frac{1}{2}|\nabla\varphi|^2 + U_x\frac{\partial\varphi}{\partial x} + U_y\frac{\partial\varphi}{\partial y} + gz\right), \tag{17}$$

where $\rho$ is the fluid density. The hydrodynamic force acting on the cylinder can be expressed as

$$F_j = \iint_{S_b} p n_j ds\ (j = 1, 2, \cdots, 6), \tag{18}$$

where $(n_1, n_2, n_3, n_4, n_5, n_6) = (n_x, n_y, n_z, r_y n_z - r_z n_y, r_z n_x - r_x n_z, r_x n_y - r_y n_x), j = 1, 2, 3$ corresponding to the force $(F_x, F_y, F_z)$ and $j = 4, 5, 6$ to the moment $(M_x, M_y, M_z)$. $\vec{r} = (r_x, r_y, r_z)$ is the position vector of any point on the cylinder surface to the center of cross section of the bottom of each cylinder. In Eq. (18), the computation of the integration $\partial\varphi/\partial t$ may cause some problems such as sawtooth type behvaviour in the force history. To overcome this difficulty, we extend the method developed by Wu and Taylor (2003), which is used in cases without current and it can circumvents the need for the derivative of the potential with respect to time directly, to the present study on wave-current-body interactions. In the fluid domain, the time derivative $\varphi_t$ satisfies the Laplace equation

$$\nabla^2\varphi_t = 0. \tag{19}$$

On the fixed boundary it satisfies

$$\frac{\partial\varphi_t}{\partial n} = 0. \tag{20}$$

On the free surface $\varphi_t$ is given by the Bernoulli equation as

$$\varphi_t = -gz - \frac{1}{2}\nabla\varphi\nabla\varphi - U_x\frac{\partial\varphi}{\partial x} - U_x\frac{\partial\varphi}{\partial y}. \tag{21}$$

Thus, $\varphi_t$ can be obtained through solving Eqs. (19)~(21).

## 3. Finite element discretization and numerical procedures

The finite element method is employed for solving the boundary value problem mentioned above. Mesh generation is an essential part of finite element based numerical simulations. In the present study, the hexahedral 20-node parametric element (see Fig. 2b) is used in the numerical simulation. The advantage of the higher-order finite element is that it has more accuracy with fewer elements than the linear 8-node element. Besides, the linear 8-node element may cause wave decaying with the development of time in some cases but the 20-node element does not. We now make a comparison of wave histories of a wave-making problem in rectangular tank in Lin et al. (1984) between using the hexahedral 20- and 8-node parametric elements. In the simulation, the length, breadth and calm water depth of the tank are $L = 9$ m, $B = 1.0$ m and $h = 0.6$ m, respectively, and they are divided into 50, 8 & 6 intervals for using the 20-node element and 200, 24 & 16 intervals for using the 8-node element, respectively, which corresponds to 2400 20-node elements and 76,800 8-node elements in the whole fluid domain. The vertical wave-maker at the left end is under a harmonic motion $X(t) = A\sin\omega t$ in the horizontal direction, where $A$ is the oscillational amplitude of the wave-maker, $\omega$ the frequency and $t$ the time. Fig. 3 gives the comparison of wave histories at 0.7 m far away the left end of the tank with $A = 0.05h$ The result through an 2D unstructured-mesh-based finite element method given by Wang and Wu (2006) is also depicted for comparison. It can be seen that the result using the 20-node element is in a good agreement with the experimental (Lin et al., 1984) and that by Wang and Wu (2006). However, the result by the 8-node element is much smaller than it. Some works (Wang and

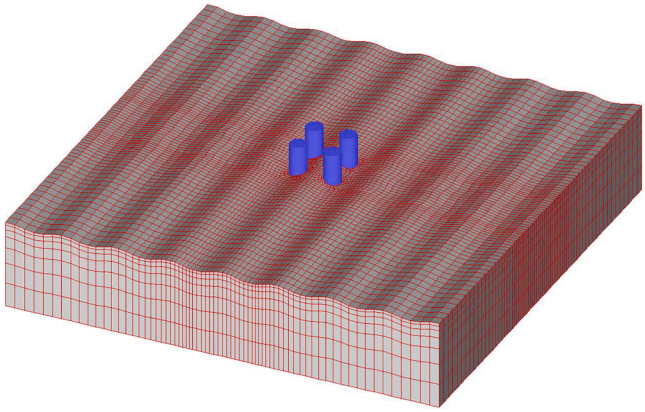

**Fig. 4.** A mesh for four bottom mounted circular cylinders.

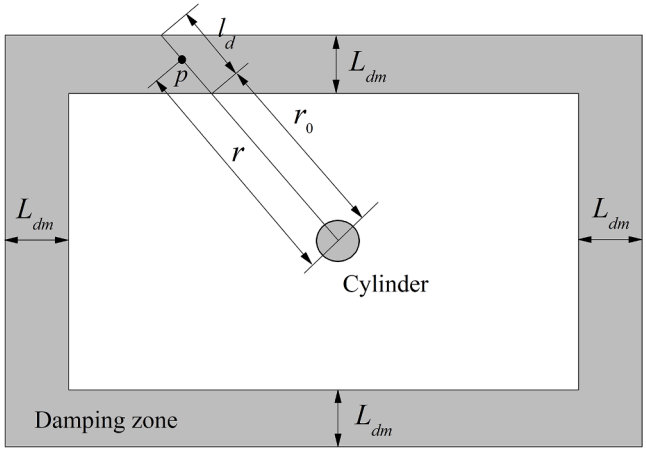


**Fig. 5.** Damping zone on free surface.

Wu, 2008; Wang et al., 2011; Wang et al., 2013; Wang and Khoo, 2005) on wave-body interactions in 2D based on higher order finite methods have been reported. The shape functions defined in a local coordinate system $\vec{\xi} = (\xi, \eta, \zeta)$ (Fig. 2a) for a standard element with twenty nodes may be expressed as

$$N_i(\xi,\eta,\zeta) = \frac{1}{8}(1+\xi\xi_i)(1+\eta\eta_i)(1+\zeta\zeta_i)(\xi\xi_i+\eta\eta_i+\zeta\zeta_i-2)\ (i=1,2,\ldots,8)$$

$$N_i(\xi,\eta,\zeta) = \frac{1}{4}(1-\xi^2)(1+\eta\eta_i)(1+\zeta\zeta_i)\ (i=9,11,13,15)$$

$$N_i(\xi,\eta,\zeta) = \frac{1}{4}(1-\eta^2)(1+\xi\xi_i)(1+\zeta\zeta_i)\ (i=10,12,14,16)$$

$$N_i(\xi,\eta,\zeta) = \frac{1}{4}(1-\zeta^2)(1+\xi\xi_i)(1+\eta\eta_i)\ (i=17,18,19,20) \tag{22}$$

this gives

$$\begin{cases} x = \sum_{i=1}^{20} x_i N_i(\xi,\eta,\zeta) \\ y = \sum_{i=1}^{20} y_i N_i(\xi,\eta,\zeta) \\ z = \sum_{i=1}^{20} z_i N_i(\xi,\eta,\zeta) \end{cases} \tag{23}$$

within any element with 20 nodes ($x_i$, $y_i$) ($i$ = 1,2,…,20) shown in Fig. 2b. A mesh with four bottom mounted circular cylinders is shown in Fig. 4. Similar to Wang and Wu (2007) and Wang and Wu (2010), an

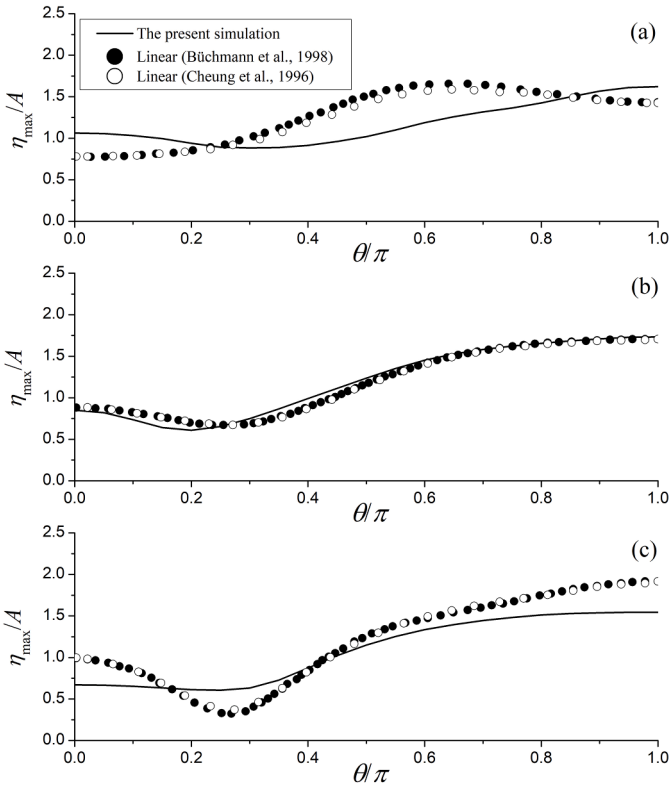


**Fig. 6.** Comparisons of wave peaks at the intersectional line; (a) $F_n$=−0.1; (b) $F_n$=0; (c) $F_n$=0.1.

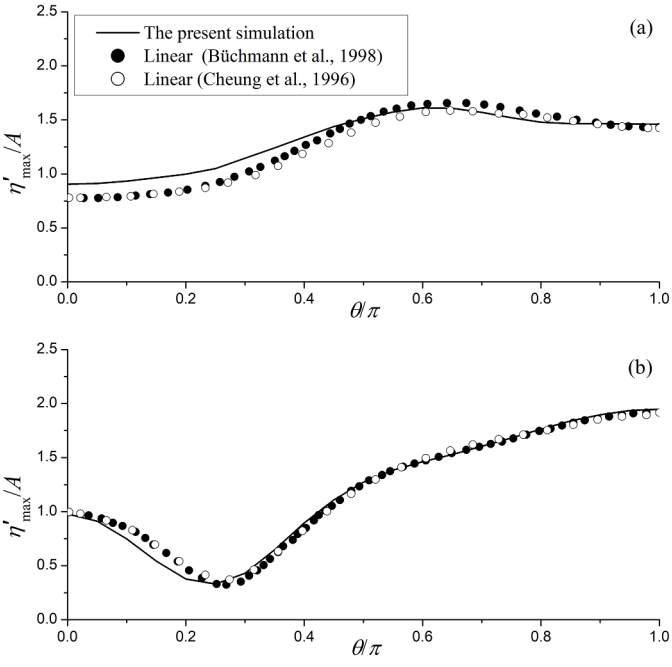


**Fig. 7.** Comparisons of wave peaks at the intersectional line; (a) $F_n$=−0.1; (b) $F_n$=0.1.

element distribution based on an equation in Chung (2002) is used to let the element to cluster near the free surface and the cylinder surface.

Once the mesh is generated, the velocity potential $\varphi$ in any element $e$ can be expressed in terms of the shape function $N_i^{(e)}(\xi,\eta,\zeta)$ in the element $e$

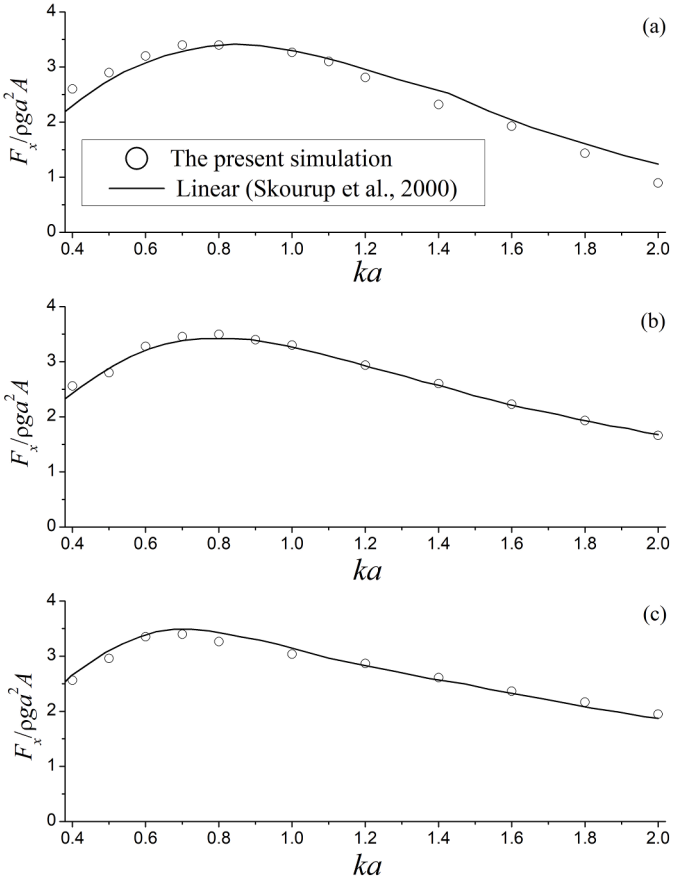


**Fig. 8.** Hydrodynamic force in $x$-direction versus $ka$; (a) $F_n$=−0.1; (b) $F_n$=0.0; (c) $F_n$=0.1.

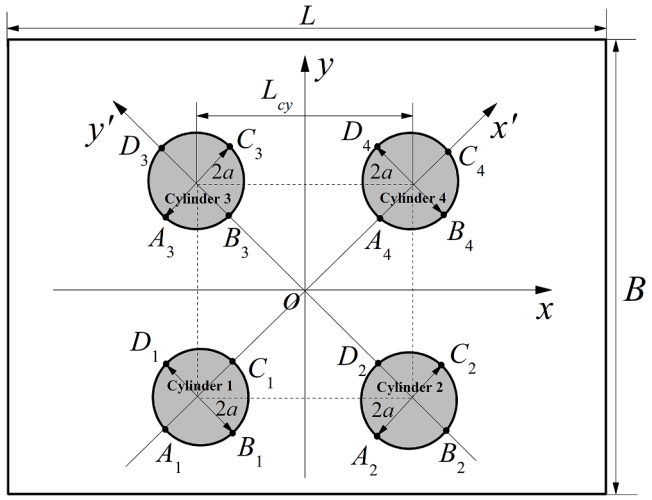


**Fig. 9.** Configuration of four cylinders.

$$\varphi(x,y,z)=\sum_{i=1}^{20}\varphi_i N_i^{(e)}(\xi,\eta,\zeta). \tag{24}$$

Through the Galerkin method, we have

$$\iiint_{\forall}\nabla^2\varphi\delta\varphi d\forall=0, \tag{25}$$

where $\delta\varphi$ is the variation of the potential. Using Green's identity and the boundary conditions, the following finite element linear system can be obtained

$$\boldsymbol{M\Phi}=\boldsymbol{F} \tag{26}$$

where $\boldsymbol{M}$ is the coefficient or stiffness matrix, $\boldsymbol{\Phi}=[\varphi_1,\varphi_2,..,\varphi_I,...,\varphi_n]^T$ is the velocity potential vector and $\boldsymbol{F}$ the right hand side vector. The element in matrix $\boldsymbol{M}$ and vector $\boldsymbol{F}$ may be expressed as, respectively,

$$M_{IJ}=\iiint_{\forall}\nabla N_I\cdot\nabla N_J d\forall$$

$$F_I=\iint_{S_n}N_I f_n dS,$$

where $N_I(\xi,\eta,\zeta)$ may be taken as a global shape function and it is expressed as

$$N_I(\xi,\eta,\zeta)=\begin{cases}N_i^{(e)}(\xi,\eta,\zeta)\ (\xi,\eta,\zeta)\ \in e\\ 0\ (\xi,\eta,\zeta)\ \notin e\end{cases},$$

and $f_n=-\vec{U}\cdot\vec{n}$ is the normal velocity on the cylinder surface given in Eq. (9). It should be mentioned that matrix $\boldsymbol{M}$ in Eq. (26) is a non-singular symmetric positive definite matrix and hence the linear system of Eq. (26) can be solved through the conjugate gradient method with a symmetric successive over relaxation (SSOR) preconditioner.

For long time simulations, an appropriate radiation condition should be imposed on the boundary $S_c$ to minimize the wave reflection. Here we use a damping zone method, which is similar to that used by Nakos et al. (1993) for the linear problem. We rewrite Eqs. (13) and (14) as

$$\frac{Dx}{Dt}=\frac{\partial\varphi}{\partial x}+U_x,\quad \frac{Dy}{Dt}=\frac{\partial\varphi}{\partial y}+U_y,\quad \frac{Dz}{Dt}=\frac{\partial\varphi}{\partial z}-\nu(r)(z-\eta_I), \tag{27}$$

$$\frac{D\varphi}{Dt}=-gz+\frac{1}{2}|\nabla\varphi|^2-\nu(r)(\varphi-\varphi_I), \tag{28}$$

where $\eta_I$ and $\varphi_I$ are the wave elevation and potential of incident wave in Eqs. (11) and (12) respectively, and $\nu$ is the damping coefficient given by

$$\nu(x)=\begin{cases}\alpha\omega\left(\dfrac{r-r_0}{l_d}\right)^2 & r_0\le r\le r_1=r_0+l_d\\ 0 & r<r_0\end{cases},$$

where $\omega$ is the linear wave frequency, and $\alpha$ is the strength of the damping coefficient and chosen to be 1.0 in this study. $r$ is the distance for the point $p$ under consideration to the center of the nearest cylinder. For a single cylinder shown in Fig. 5, damping zone starts from the edge of an inner rectangle $r=r_0(x,y)$ and ends at outer rectangle $r_1=r_0(x,y)+l_d(x,y)$. The width of the damping zone $L_{dm}$ is set to be one wavelength for short waves and eight times the radius of the cylinder cross section for long waves.

The fourth order Runge-Kutta method is adopted for the integration with respect to time to update the wave elevation and the potential on the free surface and it has been used in previous works (Wang et al., 2011; Wang et al., 2013; Wang and Khoo, 2005). In addition, when the simulation is over a substantial period of time, the nodes on the free surface may cluster and cause elements to be distorted. In order to avoid this, nodes on the free surface should be rearranged every several time steps. The element on the free surface is quadrilateral 8-node parametric. The potentials and wave elevations on all nodes of the new mesh after remeshing should be calculated through interpolation, and the first step is to calculate $(\xi,\eta)$ for each element. We define two functions $f_1(\xi,\eta)$ and $f_2(\xi,\eta)$ as follows

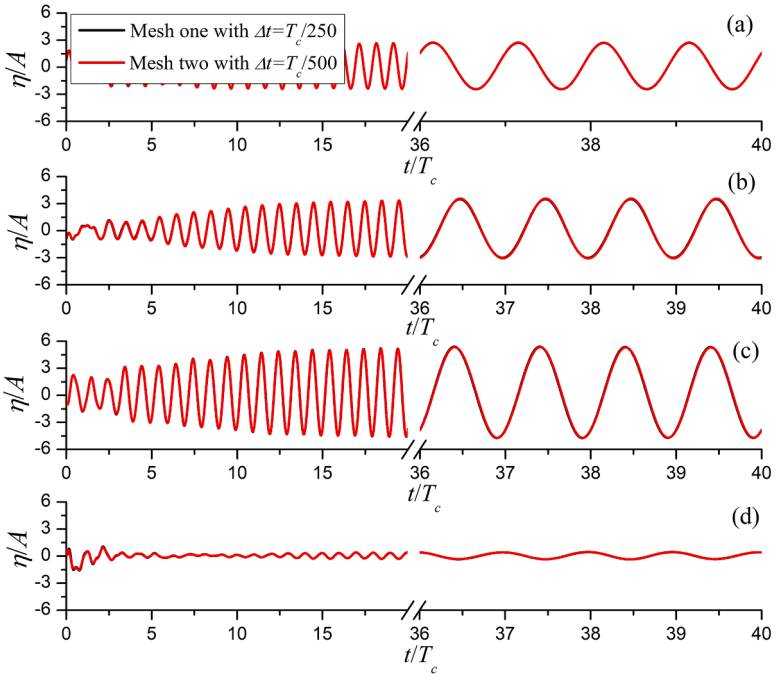


**Fig. 10.** Comparisons of wave histories at $F_n$=0.05 and $k_ca$=1.63 for two meshes with different time intervals; (a) $A_1$; (b) $C_1$; (c) $A_4$; (d) $C_4$.

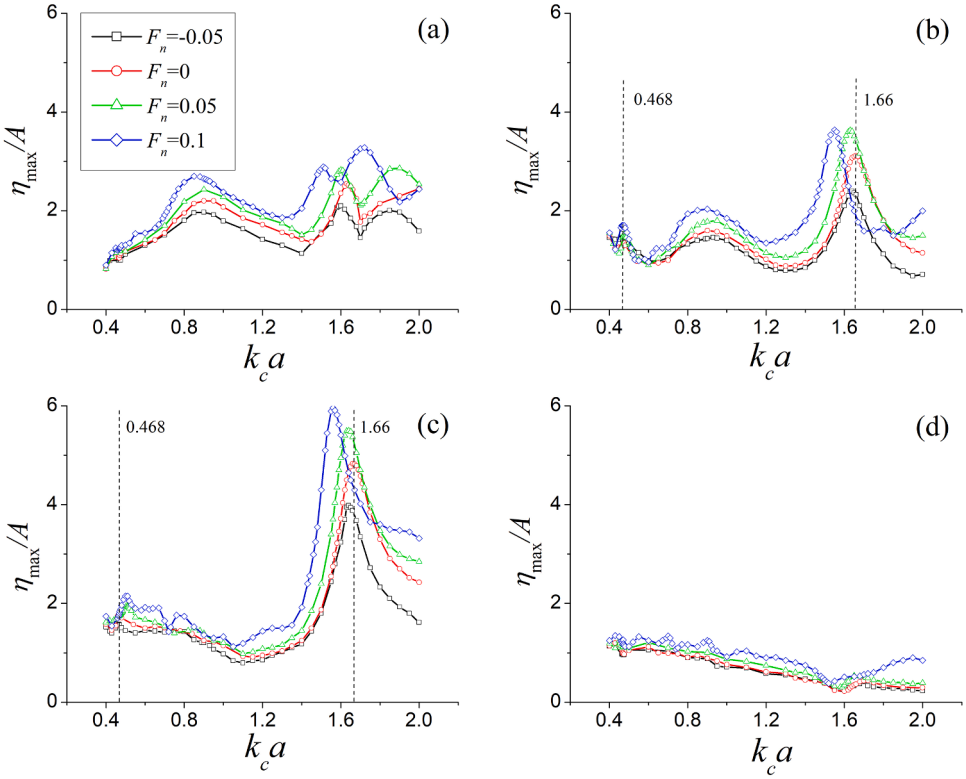


**Fig. 11.** Wave peaks versus $k_ca$ at different $F_n$; (a) $A_1$; (b) $C_1$; (c) $A_4$; (d) $C_4$.

$$\left.\begin{aligned} f_1(\xi,\eta) &= \sum_{i=1}^{8} N_i(\xi,\eta)x_i - x_r \\ f_2(\xi,\eta) &= \sum_{i=1}^{8} N_i(\xi,\eta)y_i - y_r \end{aligned}\right\}, \tag{29}$$

where $N_i(\xi,\eta)$ $(i = 1,2\ldots,8)$ are the shape functions of the quadrilateral 8-node parametric element, $(x_i, y_i)$ $(i = 1,2,\ldots,8)$ are nodes of any element before remeshing, and $(x_r,y_r)$ is any node of the new mesh. When $(x_r,y_r)$ is within the element, $(\xi,\eta)$ can be obtained by the method of Newton-kantorovich for solving the following nonlinear system

$$\boldsymbol{\xi}^{(k+1)} = \boldsymbol{\xi}^{(k)} - \boldsymbol{F}'\left(\boldsymbol{\xi}^{(k)}\right)^{-1}\boldsymbol{F}\left(\boldsymbol{\xi}^{(k)}\right) \quad (k=0,1,\cdots) \tag{30}$$

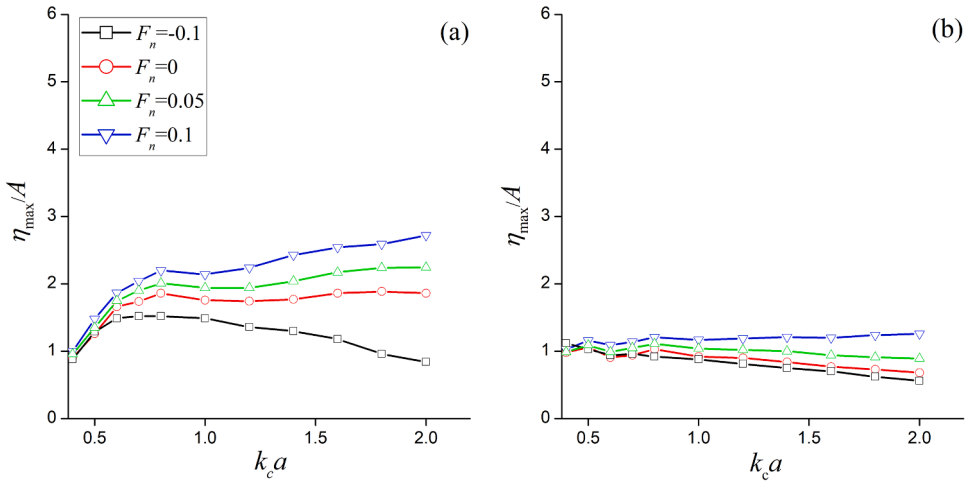


**Fig. 12.** Wave peaks versus $k_c a$ at different $F_n$ in single isolated cylinder cases; (a) Upstream side; (b) Downstream side.

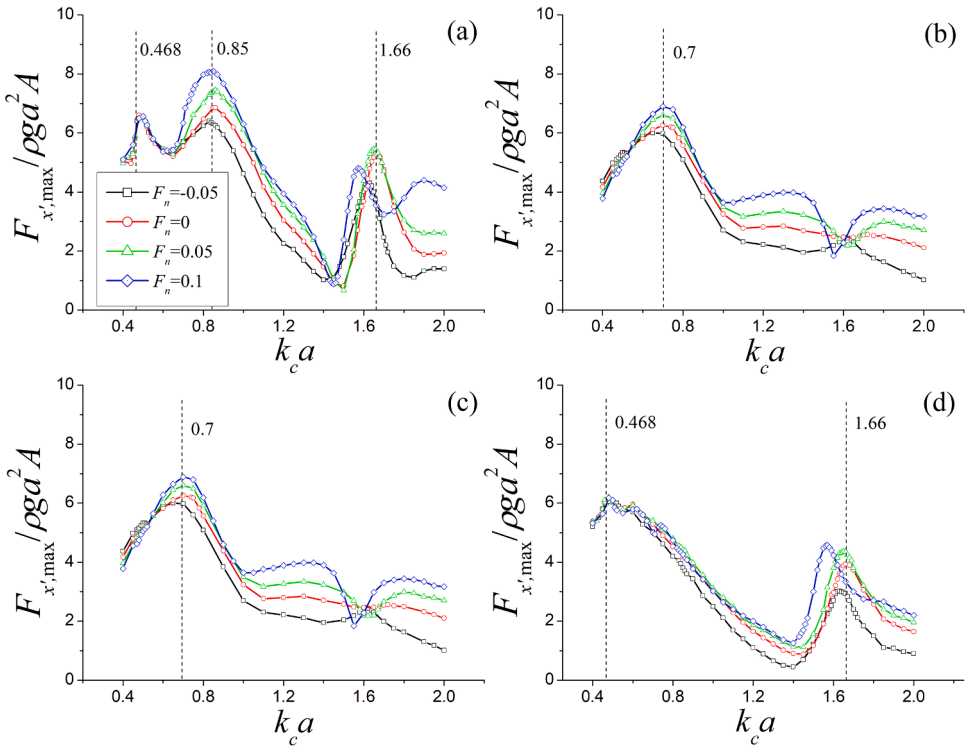


**Fig. 13.** Peaks of hydrodynamic forces in $x'$-direction versus $k_c a$ at different $F_n$; (a) Cylinder 1; (b) Cylinder 2; (c) Cylinder 3; (d) Cylinder 4.

through iteration. The superscript $(k)$ and $(k+1)$ represents the $k$- and $(k+1)$-th iterations, respectively, and $\boldsymbol{\xi}$,**F**& $\boldsymbol{F}'$are

$$\boldsymbol{\xi} = (\xi, \eta)^T,$$

$$\boldsymbol{F} = (f_1, f_2)^T,$$

$$\boldsymbol{F}'(\boldsymbol{\xi}) = \begin{bmatrix} \frac{\partial f_1}{\partial \xi} & \frac{\partial f_1}{\partial \eta} \\ \frac{\partial f_2}{\partial \xi} & \frac{\partial f_2}{\partial \eta} \end{bmatrix}.$$

respectively. The potential $\varphi_r$ and wave elevation $\eta_r$ at $(x_r, y_r)$ can be calculated after $(\xi, \eta)$ are obtained by the following equation

$$\varphi_r = \sum_{i=1}^{8} N_i(\xi, \eta)\varphi_i, \quad \eta_r = \sum_{i=1}^{8} N_i(\xi, \eta)\eta_i \tag{31}$$

where $\varphi_i$, $\eta_i$ $(i = 1,2,\ldots,8)$ are the potentials and wave elevations at $(x_i, y_i)$ $(i = 1,2,\ldots,8)$, respectively.

## 4. Numerical results

Before simulating four-cylinder cases, a single bottom-mounted cylinder whose center is at the origin and the initial water depth $h = a$, where $a$ is the cross section radius of the cylinder, is considered for

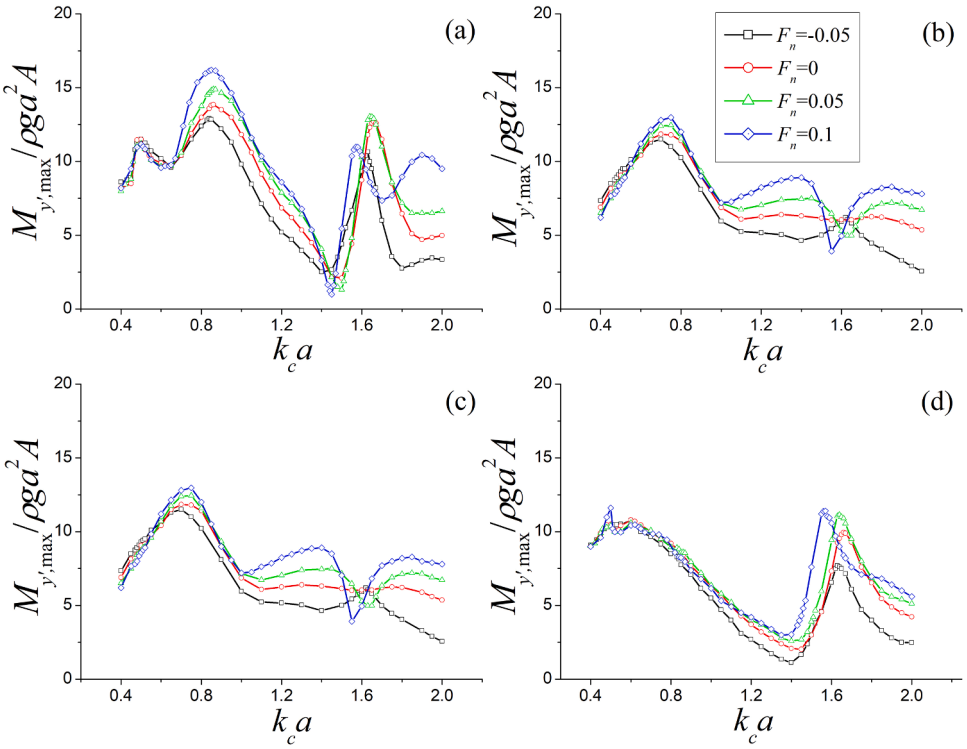


**Fig. 14.** Peaks of hydrodynamic moments around $y'$-direction versus $k_c a$ at different $F_n$; (a) Cylinder 1; (b) Cylinder 2; (c) Cylinder 3; (d) Cylinder 4.

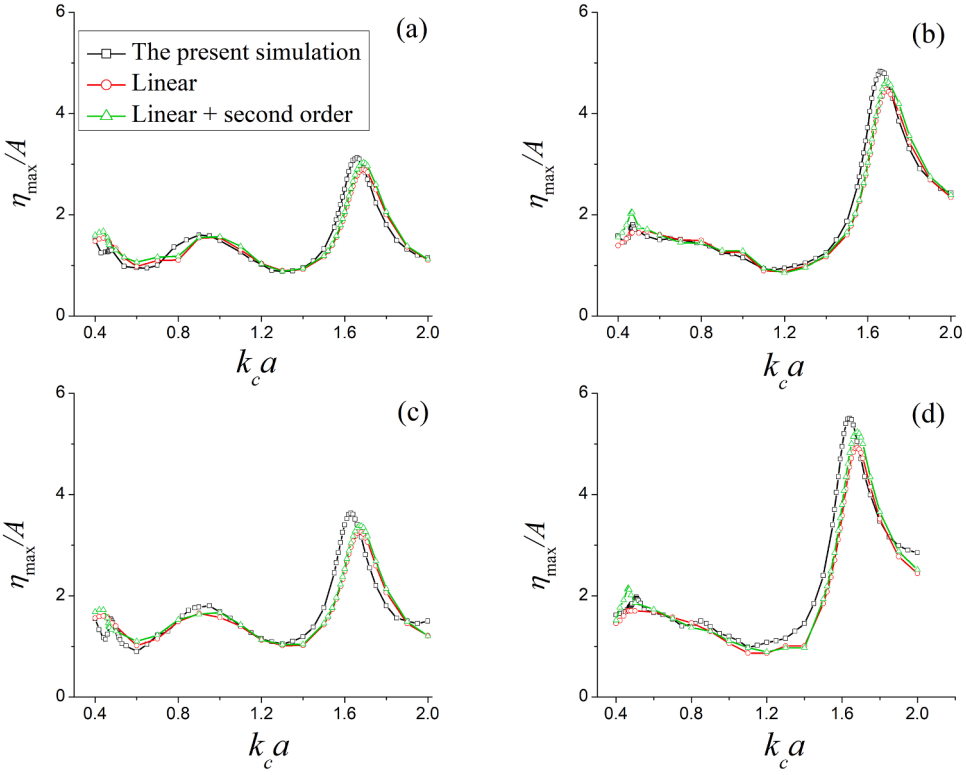


**Fig. 15.** Comparisons of wave peaks between the nonlinear results and the linear and linear plus second solutions; (a) $C_1$ ($F_n$=0); (b) $A_4$ ($F_n$=0); (c) $C_1$ ($F_n$=0.05); (d) $A_4$ ($F_n$=0.05).

validation. The incident is the second order Stokes wave and the linear wave slope $H/\lambda$=0.01. The incident angle $\beta_w = 0^o$and current angle $\beta_c = 0^o$. The nondimensionalized wavenumber $ka$=1.0, and three Froude numbers $F_n$=−0.1, 0 and 0.1 are used in the simulation. To allow a gradual development of the diffraction potential and avoid an abrupt start, a modulation or ramp function $M(t)$ is employed to the cylinder

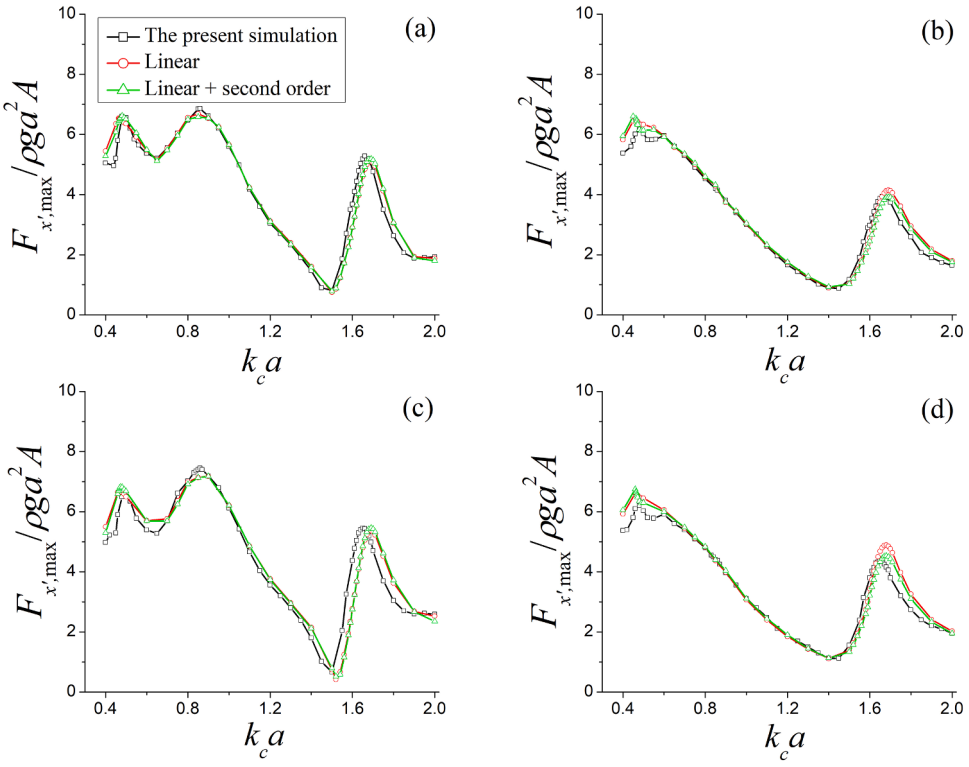


**Fig. 16.** Comparisons of hydrodynamic forces in the $x'$-direction between the nonlinear results and the linear and linear plus second solutions; (a) Cylinder 1 ($F_n$=0); (b) Cylinder 4 ($F_n$=0); (c) Cylinder 1 ($F_n$=0.05); (d) Cylinder 4 ($F_n$=0.05).

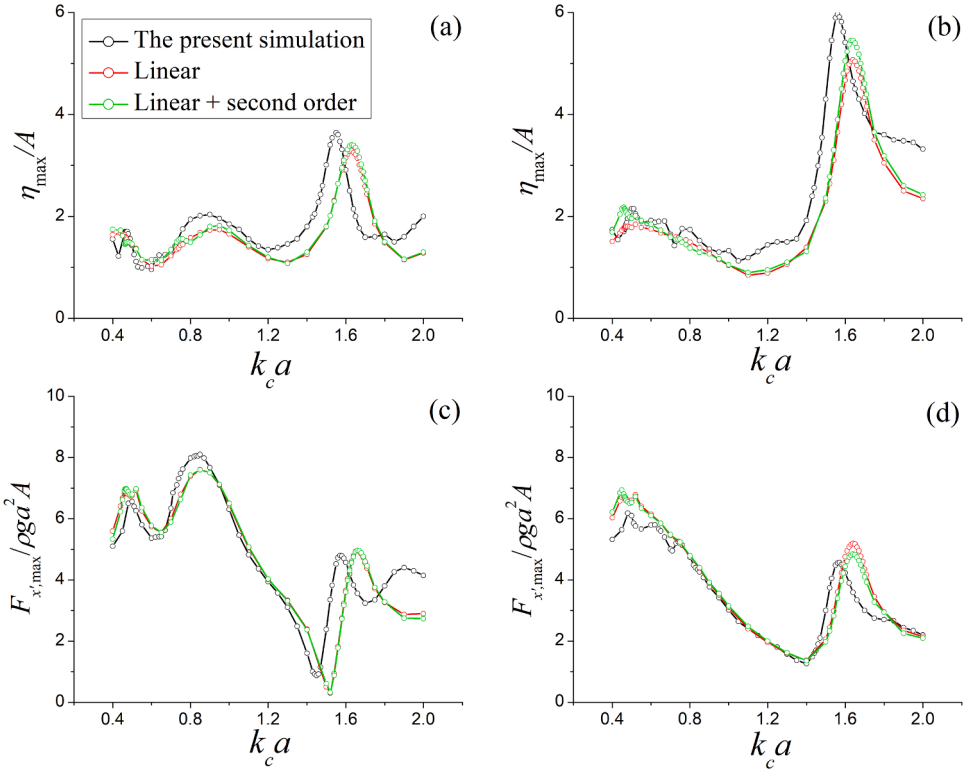


**Fig. 17.** Comparisons of wave peaks and hydrodynamic forces in the $x'$-direction between the nonlinear results and the linear and linear plus second solutions at $F_n$=0.1; (a) Wave peak at $C_1$; (b) Wave peak at $A_4$; (c) Force on cylinder 1; (d) Force on cylinder 4.

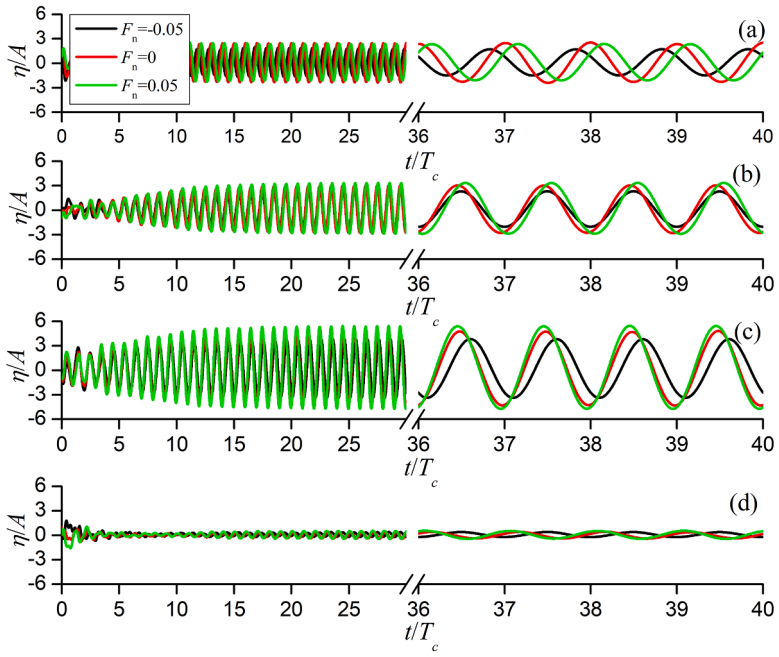


**Fig. 18.** Wave histories at $k_c a$=1.66; (a) $A_1$; (b) $C_1$; (c) $A_4$; (d) $C_4$.

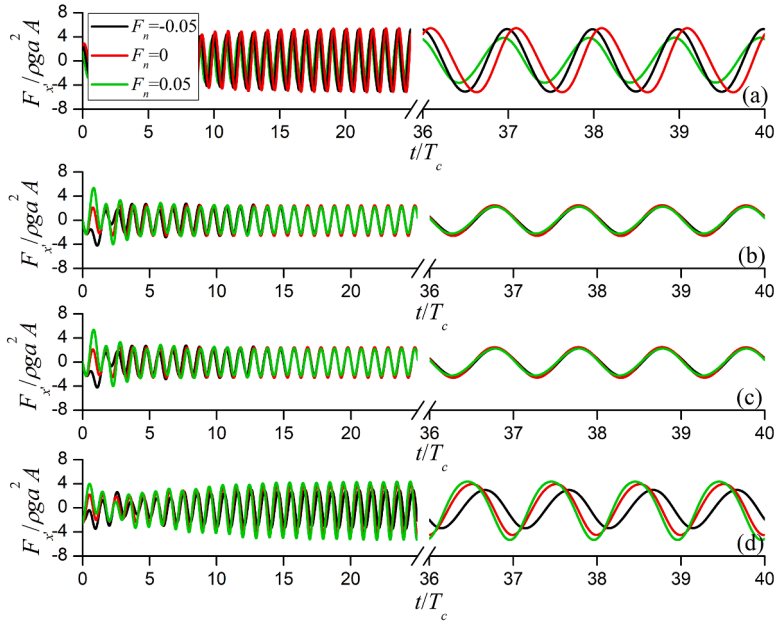


**Fig. 19.** Histories of hydrodynamic forces at $k_c a$=1.66; (a) Cylinder 1; (b) Cylinder 2; (c) Cylinder 3; (d) Cylinder 4.

surface condition given in Eq. (9)

$$\frac{\partial \varphi}{\partial n} = -M(t)\vec{U}\cdot\vec{n} \text{ on } S_b,$$

where $M(t)$ is expressed as

$$M(t) = \begin{cases} \frac{1}{2}\left[1 - \cos\left(\frac{\pi t}{T_c}\right)\right] & t < T_c \\ 1 & t \geq T_c \end{cases},$$

where $T_c$ is the linear wave period with current effect. The results about the peaks of waves around the cylinder are given in Fig. 6, in which $\theta$ is the angle between the connecting line of the original points and any intersectional point and the positive $x$-axis, and the linear results by Büchmann et al. (1998) and Cheung et al. (1996) were also provided for comparisons. It can be seen that the present fully nonlinear result is generally in good agreement with those by Büchmann et al. (1998) and Cheung et al. (1996) at $F_n$=0. However, it is clearly different from others at $F_n$=−0.1 and 0.1. This is mainly because the fully nonlinear solution includes the component of wave caused by the current and it is omitted by the linear wave theory. We now make fully nonlinear simulations without considering the wave effect. That is, interaction between the cylinder and the current only is simulated and the wave $\eta_c$ is obtained, and comparisons are then made between the linear and the fully nonlinear solutions and the results are given in Fig. 7, in which $\eta' = \eta$ for the former and $\eta' = \eta - \eta_c$ for the latter, where $\eta$ is the fully nonlinear wave in Fig. 6. The agreement becomes much better than those in Fig. 6

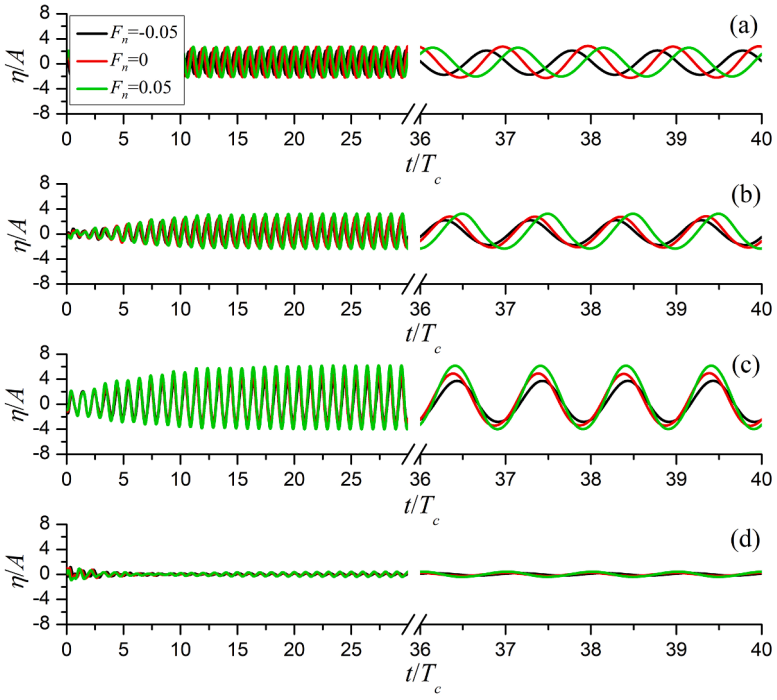


**Fig. 20.** Wave histories at $H/\lambda$=0.04 and $k_c a$=1.6;(a) $A_1$;(b) $C_1$;(c) $A_4$;(d) $C_4$.

especially at $F_n$=0.1. Fig. 8 gives comparisons of the hydrodynamic components in the $x$-direction between the present nonlinear result and the linear solution by Skourup et al. (2000) and they also agree well with each other. All these comparisons indicate that the present numerical model is effective.

The simulation is then made for wave diffraction by four vertical bottom-mounted cylinders with neighboring spacing $L_{cy}=4a$ (see Fig. 9) and the calm water depth $h = 3a$. The length and breadth of the fluid domain are $L = 8\lambda$ and $B = 8\lambda$, respectively. The coordinate system $ox'y'$ is obtained through rotating the $oxy$ by 45°. The center of the four-cylinder is at the original point $o$.

As described by Malenica et al. (1999), one of the most interesting things for the four cylinder in Fig. 9 acted by second order Stokes waves is the near-trapping phenomenon. The wave elevation at some locations and hydrodynamic forces on some cylinders become very large when the wave frequency approaches the trapped frequency. They found that the first- and second-order near-trapping modes happen at $ka$=1.66 and 0.468, respectively, when the incident wave propagates along the $x$'-axis, namely $\beta_w = 45^o$. Their work did not involve the current effect. We now consider similar cases but with considering a uniform current at $\beta_c = 45^o$ or $135^o$, which means the current along the positive or the negative $x$'-axis.

The convergence test are first made by using two meshes: one is that $n_h$=8 layers along the vertical direction and $e_f$=5044 quadrilateral 8-node elements with $n_f$=15,505 nodes on the free surface, which corresponds to $e_t$=40,352 hexahedral 20-node elements with $n_t$=181,377 nodes in the whole fluid domain, and they are $n_h$=12, $e_f$=6868, $n_f$=21,025, $e_t$=82,416 and $n_t$=358,249, respectively, for the second mesh. Fig. 10 shows wave histories at $F_n$=0.05 and $k_c a$=1.63 at four positions $A_1$, $C_1$, $B_4$ and $C_4$ by using the above two meshes with time intervals $\Delta t=T_c/250$ and $T_c/500$, respectively. It can be seen that the waves are in very good agreement for Mesh one with $\Delta t=T_c/250$ and Mesh two with $\Delta t=T_c/500$ at the four locations, which indicates that the results are convergent for using Mesh one with $\Delta t=T_c/250$.

The wave peaks at $A_1$, $C_1$, $B_4$ and $C_4$ at $H/\lambda$=0.01 and four Froude numbers $F_n$=−0.05, 0, 0.05 and 0.1 are calculated and the results about the wave peak versus $k_c a$ is given in Fig. 11, in which $\eta_{max}$ denotes the maximum value of the wave, namely the wave peak and hereinafter for the subsequent figures. The time interval in the simulation is chosen to be $\Delta t=T_c/200$ for $F_n$=0, $T_c/250$ for $F_n$=−0.05 & 0.05 and $\Delta t=T_c/500$ for $F_n$=0.1. It can be found from the Fig. 11 that the current has clear influence on the wave at these four points within the whole range of nondimensionalized wavenumber $0.4\leq k_c a\leq 2$. The variations of wave peaks with $k_c a$ is completely different from those in an isolated single cylinder cases (see Fig. 12).

As Evans and Porter (1997) pointed out, the wave energy is concentrated within the region of four cylinders especially near points $C_1$ and $A_4$ and a near trapping phenomenon happens. It can be seen that from Figs. 11b that a bigger peak appears at each Froude number at point $C_1$, which is the first trapping mode. The wave peak at $F_n$ =0 occurs at $k_c a$ =1.66, which is at the first trapping mode and obtained by the linear theory in Evans and Porter (1997) for the situation without current and also used by Malenica et al. (1999) to simulate second order wave diffraction by four bottom mounted cylinders. At smaller Froude number $F_n$=−0.05 and 0.05, the wave peaks appear around $k_c a$ =1.64 and 1.63, respectively, which are very close but slightly different from that at $F_n$=0. When the Froude number increases to a larger value $F_n$=0.1, the resonant nondimensionalized wavenumber becomes $k_c a$=1.55, which clearly deviates from those at $F_n$=−0.05, 0 and 0.05. All these indicate the resonant nondimensionalized wavenumber at $F_n\neq 0$ may be different from that $F_n$=0 and the difference becomes clearer when $F_n$ is larger. It is because the kinematic free surface condition Eq. (13) includes the term of current speed, which affects the wave evolution, and hence the wave phase may be different at different current speeds. It can also be seen that the magnitude of the peak clearly increases as the increase of the Froude number, which indicates that the wave resonance will be intensified when $F_n$ increases. From the perspective of second order theory, it should be caused by larger amplitudes of the scattered waves under larger $F_n$. This is completely different from that found by Huang and Wang (2019), in which the resonant wave produced by two cylinders in forced motions generally becomes weaker as the Froude number increases. Furthermore, a smaller peak is also observed near $k_c a$=0.468 at each Froude number, which is the second trapping mode (Malenica et al., 1999), at which the peaks are generally become larger as $F_n$ increases except those from $F_n$=−0.05 to 0. The peaks at point $A_4$ (Fig. 11c) shows similar variations

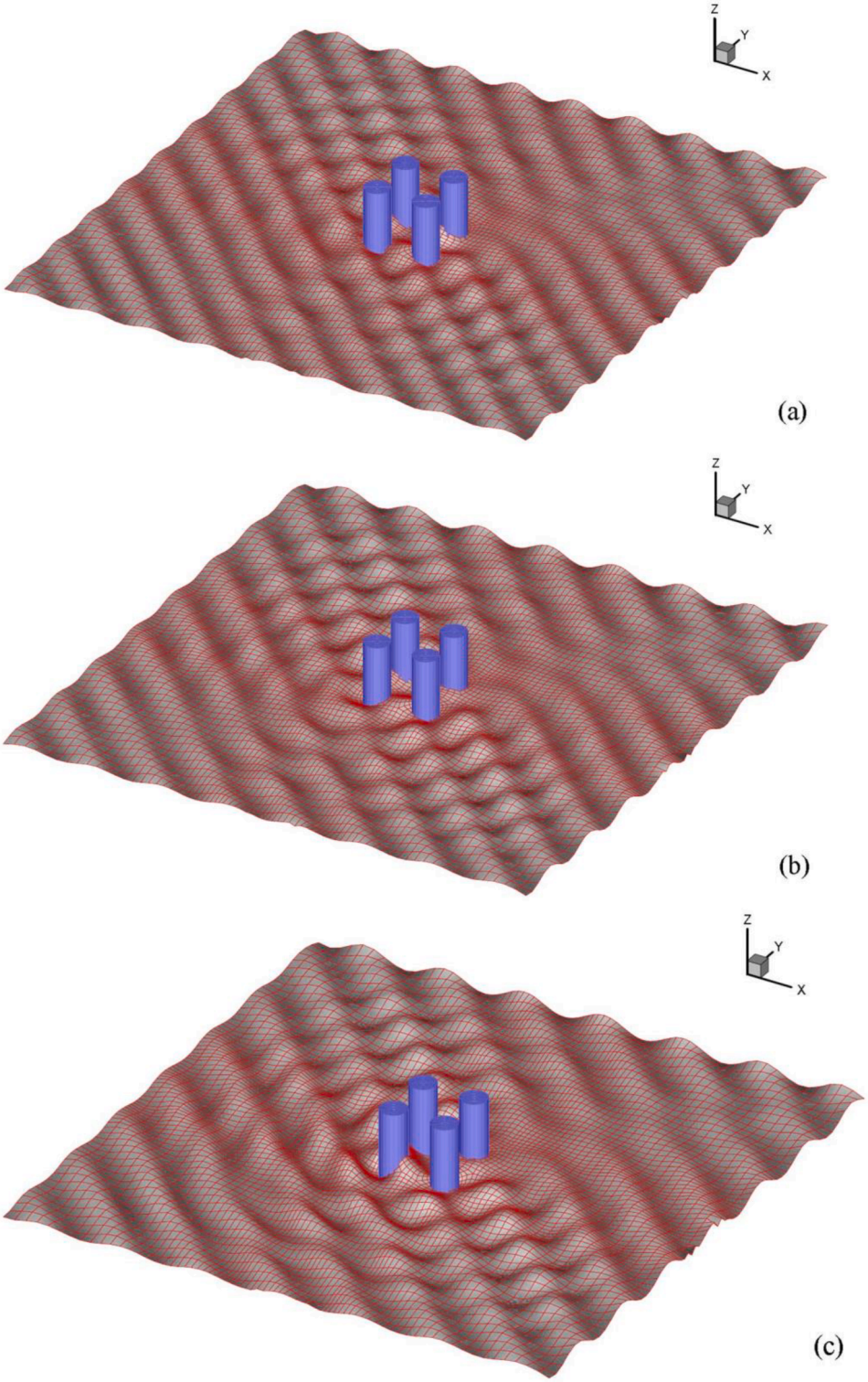


**Fig. 21.** Wave profiles at $H/\lambda$=0.02, $k_c a$=1.64 and $t$ = 25.6$T$;(a) $F_n$=−0.05;(b) $F_n$=0;(c) $F_n$=0.05.

to those at $C_1$. However, the peak shows even clearer change and it increases as the increase of $F_n$ at both the first and second trapping modes. It should be noticed that the nondimensionalized wavenumbers at the first trapping mode at $C_1$ are almost equal to those at $A_4$ but have a little more deviation at the second trapping mode. They are 0.464, 0.472, 0.476 and 0.466 at $C_1$ but 0.466, 0.472, 0.508 and 0.5 at $A_4$, respectively.

Figs. 13 and 14 depict the corresponding maxima of hydrodynamic forces in $x$'-axis and moment along $y$'-axis on four cylinders. Similar to the wave peak in Fig. 11, the difference between the four Froude numbers is clear within the whole range of nondimensionalized wavenumbers. The peaks of force at the first order trapping mode, which is near $k_c a$=1.66, can be observed, and they increase as the increase of $F_n$ from −0.05 to 0.1 for cylinder 4 and from −0.05 to 0.05 for cylinder 1. It can also be seen that smaller peaks appear around $k_c a$=0.468 at every Froude numbers for cylinders 1 and 4, which is the second trapping

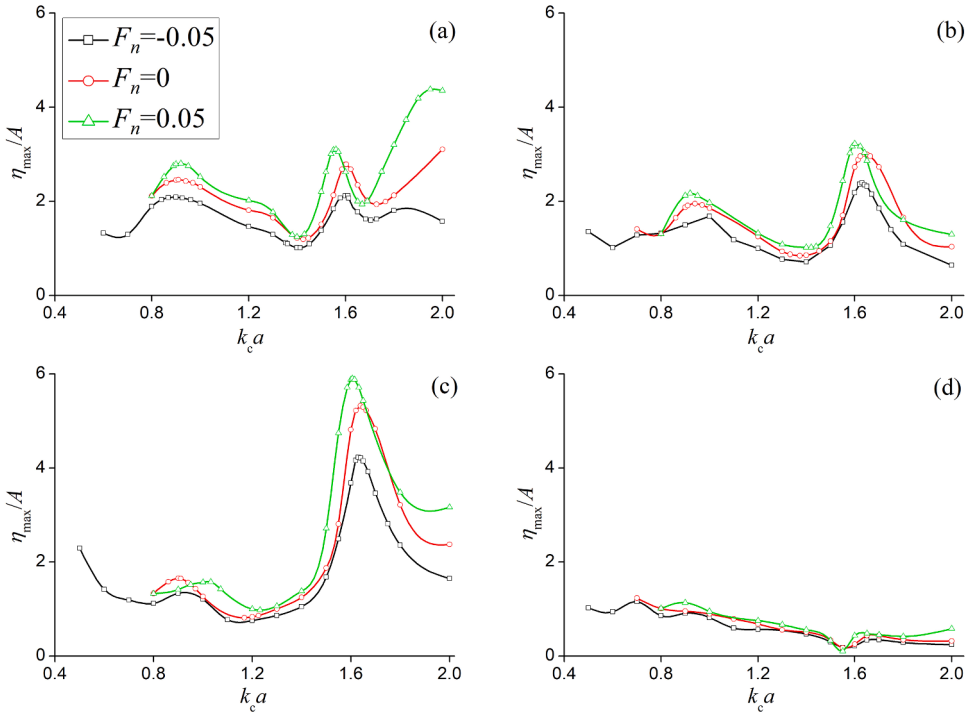


**Fig. 22.** Wave peaks versus $k_c a$ at $H/\lambda$=0.04; (a) $A_1$;(b) $C_1$;(c) $A_4$;(d) $C_4$.

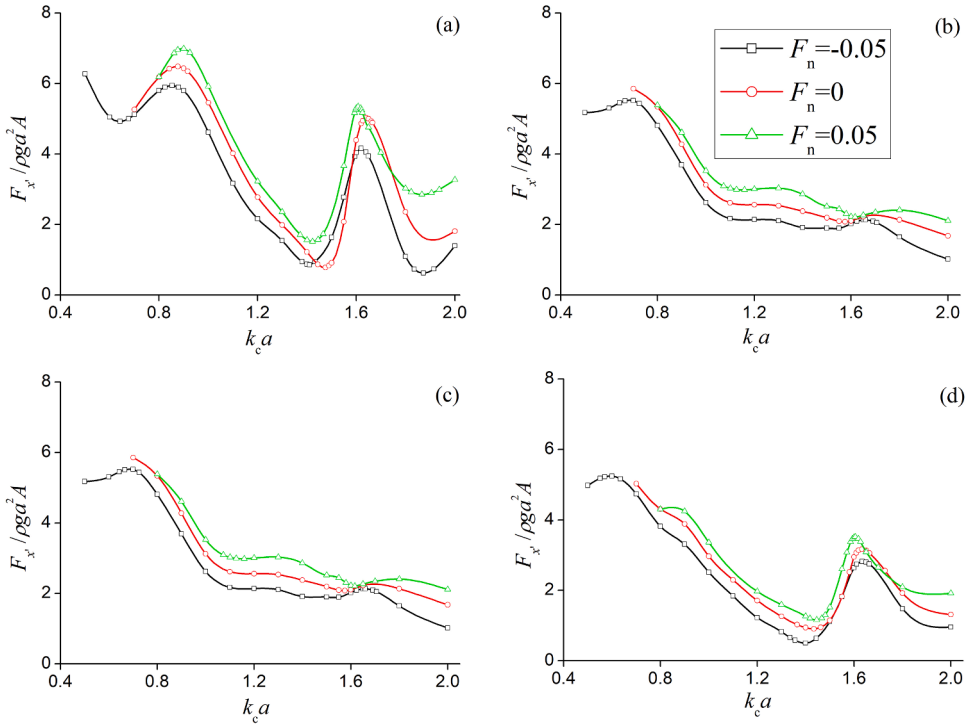


**Fig. 23.** Peaks of hydrodynamic forces in $x$'-direction versus $k_c a$ at $H/\lambda$=0.04; (a) Cylinder 1; (b) Cylinder 2; (c) Cylinder 3; (d) Cylinder 4.

mode. Actually, the largest peak for cylinders 1, 2 or 3 at each Froude number is at around $k_c a$=0.85, 0.7, respectively, and it becomes larger as the increase of $F_n$. As for the moments in Fig. 14, their variation patterns with $k_c a$ and $F_n$ are almost the same as those in Fig. 13 since the cylinder is bottom-mounted and hence the moment center does not change with the time for each cylinder. It should be noticed that cylinders 2 and 3 is symmetric about $x$'-axis and hence and the peak of force in $x$'-axis or peak of moment along $y$'-axis is identical to each other.

Fig. 15 makes comparisons of wave peaks at $C_1$ and $A_4$ between the present fully nonlinear results and those through the second order theory based on the finite element method, which has been employed by Yang and Wang (2020) for simulations of the same near-trapping phenomenon around four vertical bottom mounted cylinders in a steady current as the present paper. It is seen from the figure that the peak at the first trapping modes ($k_c a$=1.66 for $F_n$=0 and $k_c a$=1.63 for $F_n$=0.05) are a little larger than the linear plus second order solution at both $F_n$=0 and

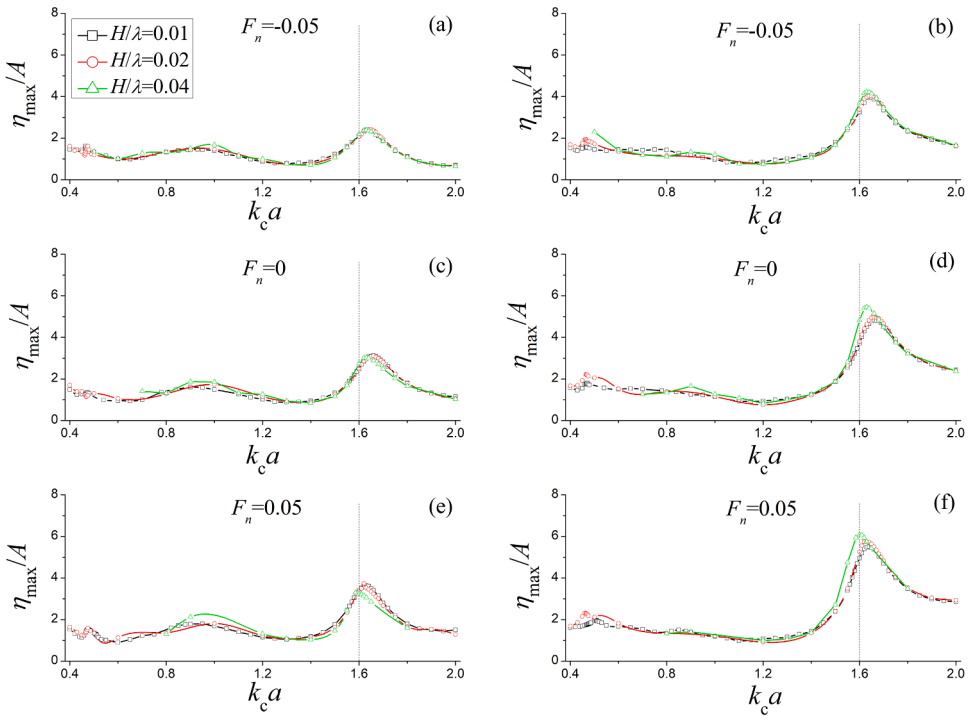


**Fig. 24.** Wave peaks versus $k_c a$ at different $H/\lambda$;(a), (c) & (e) $C_1$; (b), (d) & (f) $A_4$.

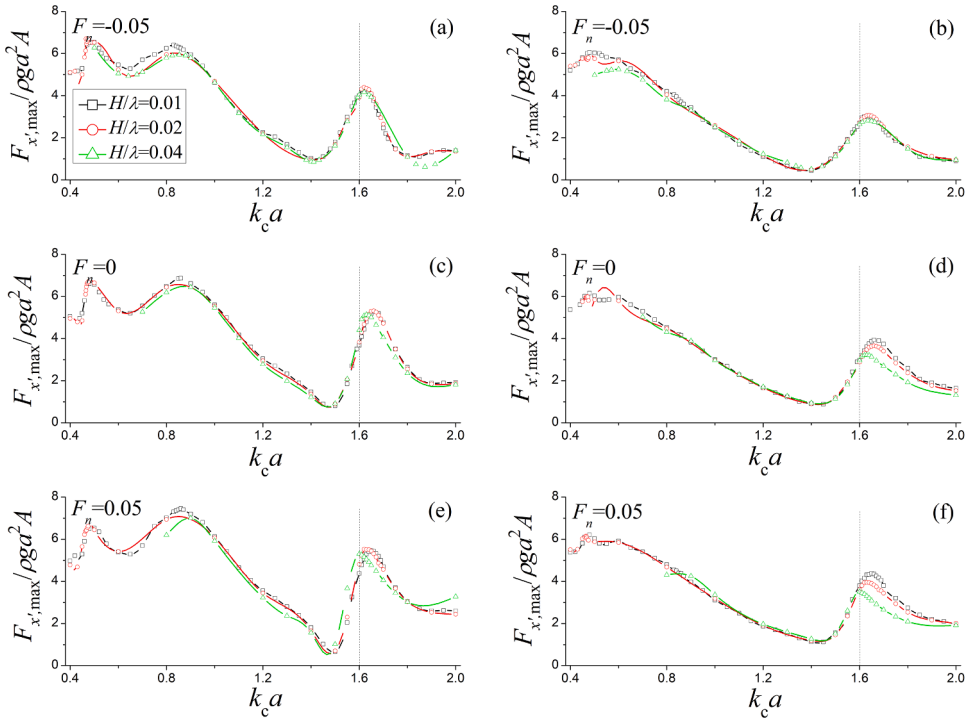


**Fig. 25.** Peaks of hydrodynamic forces on cylinders 1 & 4 versus $k_c a$ at different $H/\lambda$;(a), (c) & (e) Cylinder 1; (b), (d) & (f) Cylinder 4.

0.05, respectively. However, the fully nonlinear results are generally in good agreement at both $F_n$=0 and 0.05 with the linear plus second order solutions within the whole range of nondimensionalized wavenumber. Similarity can be found for the hydrodynamic force in the $x$'-direction in Fig. 16.

A comparison of the wave peaks and hydrodynamic forces at $F_n$=0.1 is also made and it is depicted in Fig. 17. It is seen from Figs. 17a & b that the waves at $F_n$=0.1 are clearly different from the linear plus second order solutions in magnitude and phase of peak. Through these comparisons between the fully nonlinear result and the linear plus second-order solutions at $F_n$=0, 0.05 and 0.1 in Figs. 15 and 17, it is seen that difference between them becomes larger with the increase of Froude number. This is mainly because the linear and linear plus second order solutions are based on the second order theory with the assumption of small current speed, and hence it is natural for the difference to increase as the current speed increases. The comparison of force peaks on

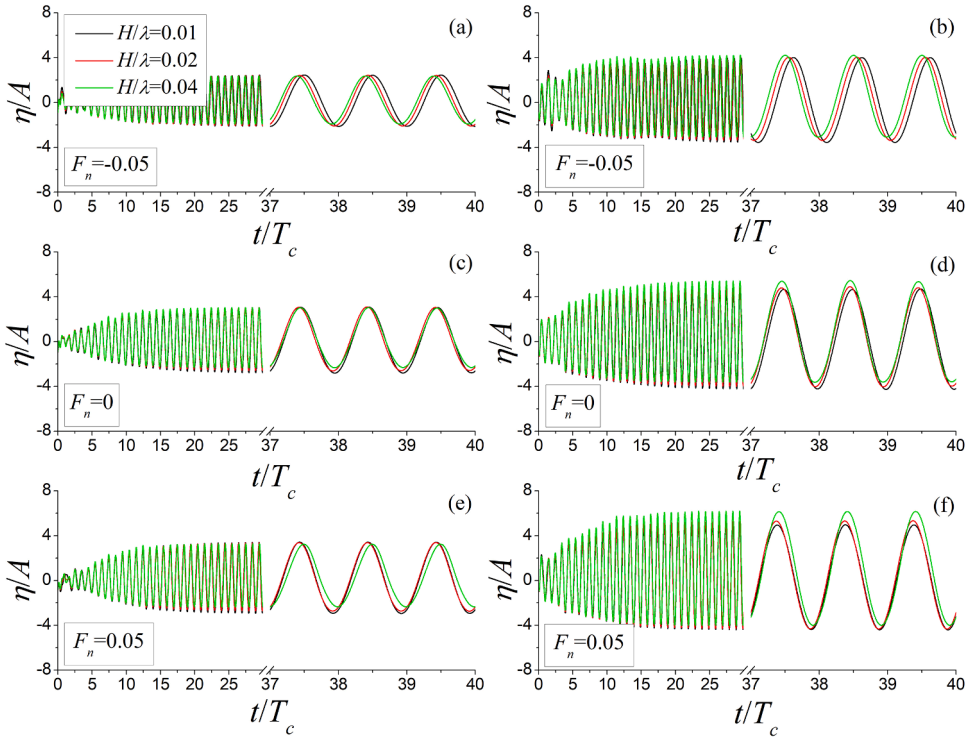


**Fig. 26.** Wave histories at (a), (b) $k_ca$=1.64 and $F_n$=−0.05;(c), (d) $k_ca$=1.64 and $F_n$=0; (e), (f) $k_ca$=1.6 and $F_n$=0.05; (a), (c) & (e) $C_1$;(b), (d) & (f) $A_4$.

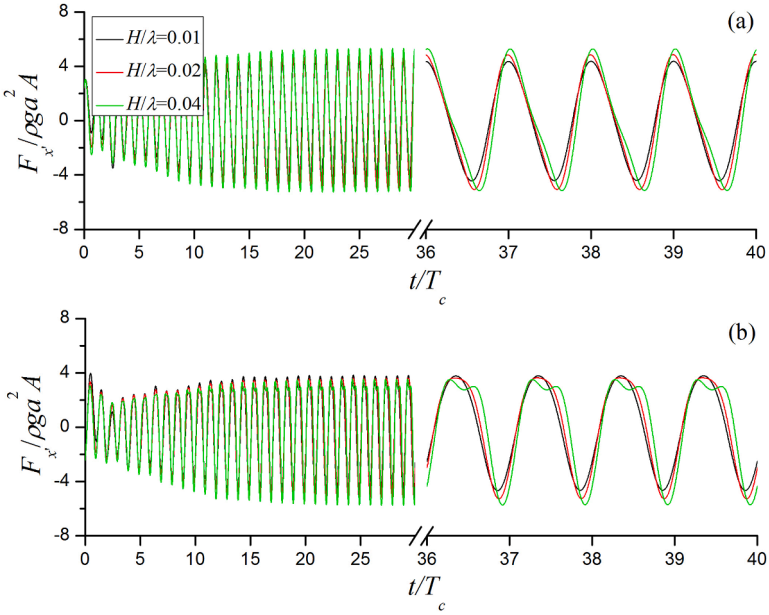


**Fig. 27.** Histories of hydrodynamic forces at $F_n$=0.05 and $k_ca$=1.6;(a) Cylinder 1;(b) Cylinder 4.

cylinders 1 & 4 in Figs. 17d & c is similar to the wave.

Fig. 18 gives histories of waves at four locations $A_1$, $C_1$, $A_4$ & $C_4$ at $k_ca$=1.66, which is close to the first trapped mode. It is seen that the waves finally become stable within 40 cycles at three Froude numbers $F_n$=−0.05, 0 & 0.05. The three waves exhibit clear difference in peaks and troughs between three Froude numbers at each location except $C_4$, and the wave peak at $C_1$ & $A_4$ becomes larger as the Froude number increases but not for that at $A_1$. In addition, the phase difference between Froude numbers generally becomes clearer with the development of time at all locations. Fig. 19 shows the corresponding hydrodynamic forces in $x$'-direction on every cylinder. It can be seen that the forces on cylinders 1 & 4 are much different from each other in peak/trough and phase between the three Froude numbers. However, they are a little difference only for those on cylinders 2 & 3 since the forces on cylinders 1 & 4 are more affected by the near-trapping mode.

We also consider some cases with two larger wave slope $H/\lambda$=0.02 and 0.04, which is at the trapping modes $k_ca$=1.64 and 1.6, respectively. We given the cases at $H/\lambda$=0.04 only here and the wave histories is plotted in Fig. 20. Similar to those at $H/\lambda$=0.01 in Fig. 18, the wave differences in peak/trough and phase between $F_n$=−0.05, 0 & 0.05 are also very clear.

The wave profiles at $H/\lambda$=0.02, $k_ca$=1.64 and $t = 25.6T$ around the

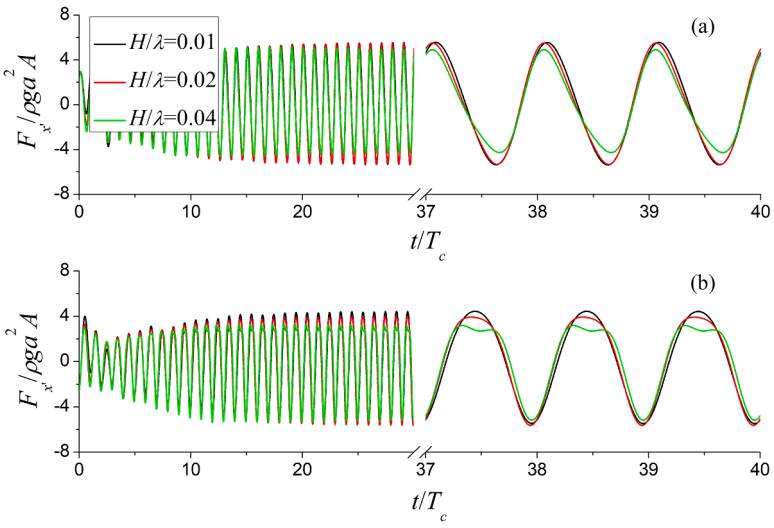


**Fig. 28.** Histories of hydrodynamic forces at $F_n$=0.05 and $k_ca$=1.64;(a) Cylinder 1;(b) Cylinder 4.

four cylinders at the near-trapping mode are plotted in Fig. 21. The wave patterns at three Froude numbers are clearly different due to current effect. It is apparently shown that six peaks within both upstream and downstream zones along the *x*'-axis direction at $F_n$=0 in Fig. 21b, but there are seven and five peaks within both zones at $F_n$=−0.05 and 0.05, respectively, which means the wavelength becomes larger as the increase of $F_n$. As discussed by Cheung et al. (1996) in their study on linear wave diffraction by a vertical bottom-mounted circular cylinder, the linear wavelengths are identical to each other at different Froude numbers when the nondimensionalized wavenumber *ka* is fixed. As shown in Fig. 21, the nondimesnional wavenumber $k_ca$ with current effect is fixed, which means *ka* decreases as $F_n$ increases, and this indicates larger wavelength at larger $F_n$. Moreover, it can also be seen that the wave peaks within the upstream zone are clearly become larger as the Froude number increases due to the larger amplitudes of the scattered waves. In addition, the waves around the cylinders are clearly different between the three Froude numbers.

The peaks of waves and hydrodynamic forces at $H/\lambda$=0.04 as functions of $k_ca$ at $F_n$=−0.05, 0 and 0.05 are given in Figs. 22 and 23. It is shown that the wave variations with $k_ca$ or $F_n$ are similar to those at $H/\lambda$=0.01 in Fig. 11, that is, the wave peaks at the near-trapping mode also becomes larger as $F_n$ increases. However, the resonant nondimensionalized wavenumbers are a little different and they are about 1.64, 1.64 and 1.6 when $F_n$=−0.05, 0 and 0.05, respectively. It can also be found that the nondimensionalized wave peaks at the resonant mode are smaller at $C_1$ and are larger at $A_4$ than those at $H/\lambda$=0.01. Similarity can be found for the force on cylinders 1 & 4 (see Figs. 23) and the moment, which is not given here.

Some comparisons of wave peaks as functions of $k_ca$ at $H/\lambda$=0.01, 0.02 and 0.04 are conducted and the wave peaks s at $C_1$ and $A_4$ are given only because they are more interesting than those at $A_1$ and $C_4$.The results are given in Fig. 24. It is seen from the figure that the changes of three peaks with $k_ca$ are similar to each other at each Froude number and each location. However, clear difference still exists within the whole range of $k_ca$ especially around the first trapping modes and it becomes even clearer at larger Froude numbers, which indicates the nonlinearity is clearer. It should be noticed that the resonant nondimensionalized wavenumbers in the simulation are a little different at different wave slopes even with identical Froude numbers, which can be seen from the figure. It can also be seen that the resonant wave peak at $C_1$ at each Froude number slowly decreases as the increase of wave slope (see Figs. 24a, c & e). In contrast to this, it clearly becomes larger when the wave slope increases at $A_4$ (see Figs. 24b, d & f). All these indicate the resonant characteristic becomes weaker at $C_1$ and it magnifies at $A_4$ as the increase of the wave slope or the incident wave amplitude.

The corresponding force peaks on both cylinders 1 and 4, on which the resonant effect is more serious than cylinders 2 and 3, are given in Fig. 25. Similar to the wave peak at $C_1$, the peaks of forces on both cylinders at the resonant frequency decreases as the increase of the wave slope at each Froude number and their discrepancy between $H/\lambda$=0.01, 0.02 and 0.04 becomes more evident at larger Froude numbers.

Figs. 26 makes further comparisons of wave histories at the resonant nondimensionalized wavenumbers $k_ca$=1.64, 1.64 and 1.6, which correspond to $F_n$=−0.05, 0 and 0.05, respectively, between $H/\lambda$=0.01, 0.02 and 0.04. At $F_n$=−0.05 and $F_n$=1.64 In Fig. 26a & b, the peak of wave at $C_1$ in Fig. 26a slightly decreases as the increase of the wave slope. On the contrary, the wave peak at $A_4$ in Fig. 26b a little clearly increases when $F_n$ becomes larger, which is consistent with those in Fig. 24. When the Froude number increases to $F_n$=0 and 0.05, the wave peak at $C_1$ (Figs. 26c, d) generally decreases as the increase of the wave slope although it not very clear. However, its increasing trend becomes more and more evident for the wave peak at $A_4$ (Figs. 26e, f).

The corresponding hydrodynamic forces on cylinders 1 and 4 are also obtained at $F_n$=0.05 and two resonant nondimensionalized wavenumbers $k_ca$=1.6 and 1.64, which correspond to $H/\lambda$= 0.04 and 0.01 or 0.02, respectively. The results are given in Figs. 27 and 28, respectively. It is seen from Fig. 27 that the forces clearly deviate from each other. It is also noticed that the force on cylinder 4 at $H/\lambda$=0.04 has double peaks, which indicates a stronger nonlinearity than others. Fig. 28 shows some similar variations to Fig. 27, in which the discrepancy between the three wave slopes is also clear. However, the difference is that the force peak regularly decreases as the wave slope increases, which can also be seen from Fig. 25.

## 5. Conclusion

The near-trapping phenomenon of wave diffraction by a four-cylinder configuration is numerically studied in the present paper. A higher order finite element with hexahedral 20-node isoperimetric elements is utilized in the fully nonlinear numerical simulations. The velocity potential in the fluid domain is obtained by solving the finite element linear system through a combination of CG method and SSOR preconditioner, while the potential and wave elevations on the free surface are updated by the fourth order Runge-Kutta method.

Validations are made for an isolated single cylinder to verify the numerical method and good agreement is achieved between the numerical results and previous studies. The fully nonlinear numerical results of waves and hydrodynamic forces for the four-cylinder have been

compared with the linear and linear plus second order solutions and it shows that they generally agree well with each other, which further verify the present numerical mode is effective.

The numerical results show that the near-trapping phenomenon is significantly affected by the uniform current. The wave peaks at some locations within the interior region of the four-cylinder increase as the Froude number increases at the first near-trapping frequencies, which indicates that the wave resonance phenomenon is intensified in the following current, namely, the Froude number $F_n>0$; In contrast to this, it is weakened in the adverse current ($F_n<0$). Similarly, the resonant characteristic of the hydrodynamic force on cylinders 1 and 4 generally becomes stronger as the Froude number increases.

The nonlinearities and resonant characteristic of waves and forces at the near-trapping modes are also studied at different wave slopes. It is found that the difference of the resonant wave peaks at both locations $C_1$ and $A_4$ at different wave slopes become more evident as the Froude number increases and hence has clearer nonlinearity. The wave peak decreases at $C_1$ and clearly increases at $A_4$ as the wave slope increases at each Froude number, which also indicates weaker and stronger resonant characteristics, respectively. However, the peak of the hydrodynamic force on both cylinders 1 & 4 at the first near-trapping mode regularly decrease as the wave slope increases at each Froude number and hence has weaker resonant characteristics.

## CRediT authorship contribution statement

**C.Z. Wang:** Writing – original draft, Project administration, Funding acquisition, Conceptualization. **J.M. Ren:** Investigation, Formal analysis, Data curation. **Y.F. Yang:** Visualization, Methodology. **H. Ge:** Writing – review & editing, Validation, Supervision.

## Declaration of competing interest

The authors declare that they have no known competing financial interests or personal relationships that could have appeared to influence the work reported in this paper.

## Data availability

Data will be made available on request.

## Acknowledgment

This work was supported by National Natural Science Foundation of China (Grant No. 52171325, 51679096), to which the authors are most grateful.

## References

Bai, W., Feng, X., Eatock Taylor, R., Ang, K.K., 2014. Fully nonlinear analysis of near-trapping phenomenon around an array of cylinders. Appl. Ocean Res. 44, 71–81.
Büchmann, B., Ferrant, P., Skourup, J., 2000. Run-up on a body in waves and current. Fully nonlinear and finite-order calculations. Appl. Ocean Res. 22 (6), 349–360.
Büchmann, B., Skourup, J., Cheung, K.F., 1998. Run-up on a structure due to second-order waves and a current in a numerical wave tank. Appl. Ocean Res. 20 (5), 297–308.
Celebi, M.S., 2001. Nonlinear transient wave–body interactions in steady uniform currents. Comput. Methods Appl. Mech. Eng. 190 (39), 5149–5172.
Chatjigeorgiou, I.K., Katsardi, V., 2018. Hydrodynamics and near trapping effects in arrays of multiple elliptical cylinders in waves. Ocean Eng. 157, 121–139.
Chen, J.T., Lee, J.W., 2013. A semi-analytical method for near-trapped mode and fictitious frequencies of multiple scattering by an array of elliptical cylinders in water waves. Phys. Fluids 25 (9), 097103.
Cheung, K.F., Isaacson, M., Lee, J.W., 1996. Wave diffraction around three-dimensional bodies in a current. ASME J. Offshore Mech. Arctic Eng. 118, 247–252.
Chung, T.J., 2002. Computational Fluid Dynamics. Cambridge University Press, pp. 543–544.
Evans, D.V., Porter, R., 1997a. Near-trapping of waves by circular arrays of vertical cylinders. Appl. Ocean Res. 19 (2), 83–99.
Evans, D.V., Porter, R., 1997b. Trapped modes about multiple cylinders in a channel. J. Fluid. Mech. 339, 331–356.
Feng, X., Bai, W., 2015. Wave resonances in a narrow gap between two barges using fully nonlinear numerical simulation. Appl. Ocean Res. 50, 119–129.
Ferrant, P., 2001. Runup on a cylinder due to waves and current: potential flow solution with fully nonlinear boundary conditions. Int. J. Offshore Polar Eng. 11 (01).
Grice, J.R., Taylor, P.H., Taylor, R.E., 2013. Near-trapping effects for multi-column structures in deterministic and random waves. Ocean Eng. 58, 60–77.
Huang, H.C., Yang, Y.F., Zhu, R.H., Wang, C.Z., 2022. Nonlinear wave resonance due to oscillations of twin cylinders in a uniform current. Appl. Ocean Res. 121, 103096.
Huang, Haocai, Wang, chizhong, 2019. Finite element simulations of second order wave resonance by motions of two bodies in a steady current. Ocean Eng. 196, 106734.
Kagemoto, H., Murai, M., Fujii, T., 2014. Second-order resonance among an array of two rows of vertical circular cylinders. Appl. Ocean Res. 47, 192–198.
Kashiwagi, M., Ohwatari, Y., 2002. First- and second-order water waves around an array of floating vertical cylinders. In: 17th International Workshop on Water Waves and Floating Bodies. Cambridge, UK.
Kim, D.J., Kim, M.H., 1997. Wave-current interaction with a large three-dimensional body by THOBEM. J. Ship Res. 41 (04), 273–285.
Koo, W., Kim, M.H., 2007. Current effects on nonlinear wave-body interactions by a 2D fully nonlinear numerical wave tank. J. Waterw. Port. Coast. Ocean. Eng. 133 (2), 136–146.
Li, Y.J., Zhang, C.W., 2016. Analysis of wave resonance in gap between two heaving barges. Ocean Eng. 117, 210–220.
Lin, W.M., Newman, J.N., Yue, D.K., 1984. Nonlinear forced motions of floating bodies. In: Proceeding of the 15th Symposium Naval Hydrodynamics. Hamburg, Germany, pp. 33–47.
Malenica, S., Taylor, R.E., Huang, J.B., 1999. Second-order water wave diffraction by an array of vertical cylinders. J. Fluid. Mech. 390, 349–373.
Maniar, H.D., Newman, J.N., 1997. Wave diffraction by a long array of cylinders. J. Fluid. Mech. 339, 309–330.
Nakos, D.E., Kring, D.C., Sclavounos, P.D., 1993. Rankine panel method for time-domain free surface flows. In: Proceeding of the 6th International Conference on Numerical Ship Hydrodynamics. Iowa, USA, pp. 614–634.
Newman, J.N., 2001. Hydrodynamics in Ship and Ocean Engineering. 3 RIAM, Kyushu University, pp. 3–26.
Ning, D.Z., SU, X.J., Zhao, M., Teng, B., 2015. Numerical study of resonance induced by wave action on multiple rectangular boxes with narrow gaps. Acta Oceanol. Sin. 34 (5), 92–102.
Ohl, C.O.G., Eatock taylor, R., Taylor, P.H., Borthwick, A.G.L., 2001. Water wave diffraction by a cylinder array. Part 1. Regular waves. J. Fluid Mech. 442, 1–32.
Shao, Y.L., Faltinsen, O.M., 2010. Numerical study on the second-order radiation/diffraction of floating bodies with/without forward speed. In: 25th International Workshop on Water Waves and Floating Bodies.
Shao, Y.L., Faltinsen, O.M., 2013. Second-order diffraction and radiation of a floating body with small forward speed. J. Offshore Mech. Arctic Eng. 135 (1), 011301.
Shivaji, G.T., Sen, D., 2016. Time domain simulation of side-by-side floating bodies using a 3D numerical wave tank approach. Appl. Ocean Res. 58, 189–217.
Skourup, J., Cheung, K.F., Bingham, H.B., Büchmann, B., 2000. Loads on a 3D body due to second-order waves and a current. Ocean Eng. 27 (7), 707–727.
Ursell, F., 1951. Trapping modes in the theory of surface waves. In: Mathematical Proceedings of the Cambridge Philosophical Society. Cambridge University Press.
Walker, D.A.G., Taylor, R.E., 2005. Wave diffraction from linear arrays of cylinders. Ocean Eng. 32 (17–18), 2053–2078.
Walker, D.A.G., Taylor, R.Eatock, Taylor, P.H., Zang, J., 2008. Wave diffraction and near-trapping by a multi-column gravity-based structure. Ocean Eng. 35 (2), 201–229.
Wang, C.Z., Huang, H.C., Meng, Q.C., Khoo, B.C., 2013. Finite element analysis of nonlinear wave resonance by multiple cylinders in vertical motions. Comput. Fluids. 88, 557–568.
Wang, C.Z., Khoo, B.C., 2005. Finite element analysis of two-dimensional nonlinear sloshing problems in random excitations. Ocean Eng. 32 (2), 107–133.
Wang, C.Z., Wu, G.X., 2006. An unstructured mesh based finite element simulation of wave interactions with non-wall-sided bodies. J. Fluids. Struct. 22, 441–461.
Wang, C.Z., Wu, G.X., 2007. Time domain analysis of second-order wave diffraction by an array of vertical cylinders. J. Fluids. Struct. 23 (4), 605–631.
Wang, C.Z., Wu, G.X., 2008. Analysis of second order resonance in wave interactions with floating bodies through a finite element method. Ocean Eng. 35, 717–726.
Wang, C.Z., Wu, G.X., 2010. Interactions between fully nonlinear water waves and an array of cylinders in a wave tank. Ocean Eng. 37, 400–417.
Wang, C.Z., Wu, G.X., Khoo, B.C., 2011. Fully nonlinear simulation of resonant motion of liquid confined between floating structures. Comput. Fluids 44, 89–101.
Wu, G.X., Ma, Q.W., taylor, R.Eatock, 1998. Numerical simulation of sloshing waves in a 3D tank based on a finite element method. Appl. Ocean Res. 20, 337–355.
Wu, G.X., Taylor, R.Eatock, 2003. The coupled finite element and boundary element analysis of nonlinear interactions between waves and bodies. Ocean Eng. 30, 387–400.
Yang, Y.F., Wang, C.Z., 2020. Finite element analysis of second order wave resonance by multiple cylinders in a uniform current. Appl. Ocean Res. 100, 102132.